Chemistry and Materials

The Center for Science Innovation

Research Article

Chem. Mater. 5 (2) 2026, 95-107

Dense Granular vs Sparse Agglomerated Morphology in Ni–Fe–Sn Electrocatalysts for Ethanol Oxidation Reaction

Juliandi Siregar[1], Muhammad Fathar Aulia[2,*]

[1]Department of Physics Education, Universitas Muslim Nusantara Al-Washliyah, Medan 20147, Indonesia

[2]The Center for Science Innovation Arva Building, Jl. RP. Soeroso, Jakarta 10350, Indonesia

*Corresponding author: m.fathar@piscience.org

Received
18 May 2026

Received in revised form
24 June 2026

Accepted
26 June 2026

Published online
30 June 2026

DOI
https://doi.org/10.56425/cma.v5i2.142

Abstract

The development of efficient and durable non-noble-metal electrocatalysts for the ethanol oxidation reaction (EOR) remains challenging due to limitations associated with sluggish kinetics and catalyst poisoning. Herein, a morphology-driven strategy is proposed to elucidate the role of granular and compact architectures in governing the electrocatalytic performance of ternary Ni–Fe–Sn catalysts. NiFeSn electrocatalysts were synthesized via potentiostatic electrodeposition. This work provides a comparative investigation of how morphological evolution influences interfacial kinetics, catalytic activity, and operational stability during EOR. Scanning electron microscopy (SEM) analysis revealed that NiFeSn(A) possessed a densely packed granular morphology with uniformly distributed quasi-spherical particles, whereas NiFeSn(B) exhibited sparse surface coverage and localized agglomeration. Electrochemical evaluation demonstrated that NiFeSn(A) achieved superior EOR performance with a peak current density of 117.61 mA cm^{-2}, 1.60-fold higher than NiFeSn(B) (73.47 mA cm^{-2}), together with a lower onset potential (570 mV), lower charge-transfer resistance (2.84 Ω after cycling), and smaller Tafel slope (33.26 mV dec^{-1}). Furthermore, NiFeSn(A) exhibited enhanced poisoning tolerance and improved long-term stability during chronoamperometric measurements. The superior performance of NiFeSn(A) is attributed to its interconnected granular morphology, which promotes charge-transfer kinetics, active-site accessibility, and efficient oxidative removal of poisoning intermediates, highlighting morphology engineering as an effective route for developing high-performance Ni-based EOR electrocatalysts.

Keywords: EOR, morphology-dependent catalysis, Ni–Fe–Sn catalyst

1. Introduction

Fuel cells are highly efficient energy conversion devices that directly convert chemical energy into electricity through electrochemical reactions, offering an environmentally friendly alternative to conventional energy technologies [1–3]. Among them, *direct ethanol fuel cells* (DEFCs) have attracted considerable attention because ethanol possesses high energy density, low toxicity, and can be sustainably produced from biomass and agricultural waste [4]. However, the practical implementation of DEFCs is hindered by the inherently sluggish ethanol oxidation reaction (EOR). Besides requiring complex multi-electron transfer and C–C bond cleavage, EOR faces additional challenges related to low product selectivity, the formation of strongly adsorbed intermediate species, and catalyst poisoning, all of which reduce reaction efficiency and long-term stability [5,6]. Since the electrode serves as the active site for electrochemical reactions in DEFCs [7], the development of highly active and durable electrocatalysts is essential for improving their overall performance.

Platinum-based catalysts are widely employed for EOR owing to their excellent catalytic activity [8]. However, their practical application is limited by high cost and

vulnerability to poisoning by CO-containing intermediates, resulting in decreased activity and durability [9,10]. Consequently, the development of low-cost and efficient non-noble metal catalysts has become a major research focus. Among them, nickel (Ni) is considered a promising candidate because of its natural abundance and low cost [11]. Ni-based electrocatalysts exhibit appreciable activity toward ethanol oxidation owing to their good electrical conductivity, thermal stability, and favorable electrochemical propertie [12]. In alkaline media, Ni species are readily transformed into electroactive Ni(III) species, such as NiOOH, which act as oxidation mediators by providing active oxygen species that facilitate the oxidation of ethanol and its adsorbed intermediates [13]. Nevertheless, the catalytic performance of pure Ni remains inferior to that of noble metals, resulting in lower EOR performance.

Alloying Ni with other metals can generate synergistic effects that enhance catalytic performance beyond that of monometallic Ni [14]. Among various promoters, iron (Fe) is widely incorporated into Ni-based catalysts because of its low cost and its ability to modify the electronic structure and redox environment of Ni, thereby facilitating charge transfer and improving electrical conductivity [15][16]. Nevertheless, excessive Fe incorporation has been reported to suppress the $Ni(OH)_2$/NiOOH redox transition and shift the oxidation onset potential [17]. To overcome these limitations, the incorporation of tin (Sn) has been proposed as an effective strategy. Ni acts as the primary redox-active center through the formation of NiOOH species, Fe enhances electron transfer by tuning the electronic structure of Ni, and Sn provides oxophilic sites that facilitate OH adsorption and the oxidative removal of strongly adsorbed intermediates [18][19]. These synergistic effects improve catalytic activity, making Ni–Fe–Sn catalysts promising candidates for ethanol oxidation reactions.

Since the catalytic performance of multimetallic systems is strongly influenced not only by their composition but also by their surface structure, considerable efforts have been devoted to developing suitable synthesis strategies for controlling catalyst morphology. Various methods, including hydrothermal, sol–gel, and wet impregnation techniques, have been reported for electrocatalyst preparation; however, these approaches often involve complex procedures and prolonged processing times. Electrodeposition offers a simpler, cost-effective, and efficient alternative, with the additional advantage of precise control over the nucleation and growth of metal particles [20]. In particular, potentiostatic electrodeposition enables the regulation of film growth and surface morphology through the applied potential [21]. The applied potential governs the nucleation rate, growth kinetics, surface coverage, and elemental composition of the deposited layer, thereby providing an effective means to tailor the physicochemical properties and catalytic performance of multimetallic electrocatalysts [22].

Although Ni-based and multimetallic catalysts have been extensively investigated for ethanol oxidation, the influence of different surface architectures on catalytic behavior remains insufficiently understood. In particular, a systematic comparison between dense granular and sparse agglomerated morphologies is still lacking. Such a comparison is necessary because these distinct structures provide different degrees of surface exposure, electrolyte accessibility, and mass transport, which can strongly affect ethanol adsorption, intermediate oxidation, and charge-transfer kinetics during the ethanol oxidation reaction (EOR) [23]. Therefore, this work aims to establish the morphology–activity relationship of ternary Ni–Fe–Sn electrocatalysts by comparatively investigating catalysts with dense granular and sparse agglomerated morphologies toward EOR.

2. Materials and Method

2.1. Material

All chemicals used in this study were of analytical grade purity. Nickel (II) sulfate hexahydrate ($NiSO_4 \cdot 6H_2O$), iron (II) sulfate heptahydrate ($FeSO_4 \cdot 7H_2O$), tin (II) chloride ($SnCl_2$), sodium chloride (NaCl), and sodium citrate dihydrate ($Na_3C_6H_5O_7 \cdot 2H_2O$) were purchased from Merck. Boric acid (H_3BO_3), hydrochloric acid (HCl), potassium hydroxide (KOH), ethanol (C_2H_5OH), and deionized water were used in this study.

2.2. Synthesis of Ni–Fe–Sn Electrocatalysts

Ni–Fe–Sn electrocatalysts were synthesized via a potentiostatic electrodeposition method using a conventional three-electrode system. Copper (Cu) foil (0.15 mm thickness) was employed as the substrate. Prior to deposition, the Cu substrate (3 × 1 cm) was mechanically polished with abrasive paper to obtain a smooth surface, followed by ultrasonic cleaning in deionized water for 20 min. The substrate was then rinsed with ethanol and deionized water, and dried at room temperature. The electrolyte solution was prepared by dissolving 0.076 M $NiSO_4 \cdot 6H_2O$, 0.022 M $FeSO_4 \cdot 7H_2O$, and 0.004 M $SnCl_2$ (pre-dissolved in 0.08 mL of 67% HCl). Subsequently, 0.1 M H_3BO_3 was added as a buffering agent, 0.1 M $Na_3C_6H_5O_7 \cdot 2H_2O$ as a complexing agent, and 0.04 M NaCl

to enhance electrolyte conductivity. Electrodeposition was performed potentiostatically for 20 min at room temperature without pH adjustment or mechanical stirring. Two NiFeSn electrocatalysts with distinct surface morphologies were synthesized by varying the applied potential. NiFeSn(A) was deposited at −1.0 V, resulting in a dense granular morphology, whereas NiFeSn(B) was deposited at −1.2 V, producing a sparse agglomerated morphology. After deposition, the electrodes were rinsed with deionized water and dried prior to further characterization.

2.3. Characterization

The surface morphology and elemental composition of the electrocatalysts were analyzed using scanning electron microscopy (SEM, JEOL JSM-IT200) equipped with energy-dispersive X-ray spectroscopy (EDX). SEM imaging was conducted at an accelerating voltage of 10–12 kV, while EDX analysis was performed at 20 kV.

2.4. Electrochemical Measurements

The electrocatalytic performance toward ethanol oxidation was investigated using cyclic voltammetry (CV), linear sweep voltammetry (LSV), electrochemical impedance spectroscopy (EIS), and chronoamperometry (CA) measurements performed on a CorrTest CS310 electrochemical workstation. All electrochemical tests were conducted in an electrolyte containing 1 M KOH and 1 M ethanol. CV measurements were carried out within a potential range of 0 – 1.0 V (vs. Ag/AgCl) at a scan rate of 200 mV s^{-1} for 1000 cycles to evaluate the catalytic activity and long-term durability. LSV measurements were recorded at a scan rate of 10 mV s^{-1} to examine the ethanol oxidation kinetics. EIS measurements were performed at 0.65 V (vs. Ag/AgCl) over a frequency range from 100 kHz to 0.1 Hz to assess the charge-transfer characteristics of the samples. In addition, the catalytic stability was further evaluated by chronoamperometry at 0.65 V (vs. Ag/AgCl) for 3600 s.

3. Results and Discussion

The surface morphology of the deposited films was examined by FESEM, as shown in Fig. 1. NiFeSn(A), deposited at −1.0 V, exhibits a dense granular morphology consisting of uniformly distributed quasi-spherical particles with cauliflower-like features that are closely packed across the substrate surface. The high surface coverage and relatively homogeneous particle size indicate that deposition at this potential promotes balanced nucleation and growth, resulting in a continuous and interconnected structure [24]. In contrast, NiFeSn(B), deposited at −1.2 V, displays a sparse agglomerated morphology characterized by isolated spherical clusters and substantial uncovered regions of the substrate. Compared with NiFeSn(A), the particle distribution is considerably less uniform, and the surface coverage is markedly reduced [25]. The morphological transition from a dense granular structure to a sparse agglomerated architecture suggests that increasing the cathodic overpotential alters the nucleation and growth behavior, leading to localized particle growth and non-uniform deposition. Such differences in surface architecture are expected to influence the number of accessible active sites, electrolyte penetration, and charge-transfer processes, thereby affecting the electrocatalytic performance of the NiFeSn catalysts toward ethanol oxidation.

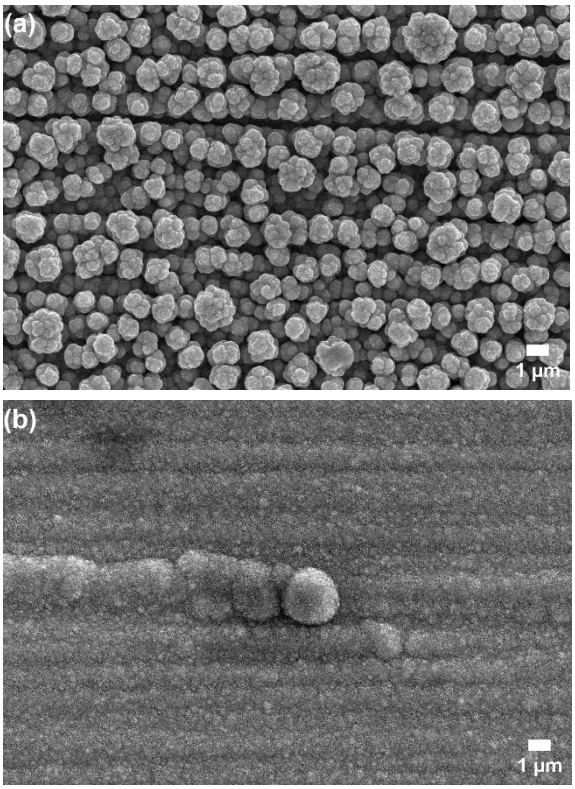

Figure 1. SEM results of (a) NiFeSn(A) and (b) NiFeSn(B).

Moreover, the chemical composition of the electrocatalysts was investigated using EDX, confirming the successful co-deposition of Ni, Fe, and Sn elements in both samples. As summarized in Table 1, NiFeSn(A) consists of 57.44 at.% Ni, 35.40 at.% Fe, and 7.15 at.% Sn, whereas NiFeSn(B) contains a higher Ni concentration of 64.77 at.% accompanied by lower Fe (31.01 at.%) and Sn (4.22 at.%) contents. The compositional evolution observed at the more negative deposition potential indicates that Ni incorporation becomes increasingly dominant under higher cathodic overpotential, while the

incorporation of Fe and especially Sn is progressively reduced, resulting in the formation of a more Ni-rich alloy.

Table 1. Elemental composition and elemental ratio of NiFeSn catalyst.

Sample	wt.%			Ni/Fe	Ni/Sn	Ni/Fe+Sn	at.%			Ni/Fe	Ni/Sn	Ni/Fe+Sn
	Ni	Fe	Sn				Ni	Fe	Sn			
NiFeSn(A)	54.4	31.9	13.7	1.71	3.97	1.19	57.44	35.40	7.15	1.62	8.03	1.35
NiFeSn(B)	63.0	28.7	8.3	2.20	7.59	1.71	64.77	31.01	4.22	2.09	15.35	1.84

To further evaluate the elemental incorporation behavior, the atomic ratios of Ni/Fe, Ni/Sn, and Ni/(Fe+Sn) were calculated. NiFeSn(A) exhibited ratios of 1.62, 8.03, and 1.35, respectively, whereas NiFeSn(B) showed higher values of 2.09, 15.35, and 1.84. The substantial increase in the Ni/Sn and Ni/(Fe+Sn) ratios for NiFeSn(B) indicates a pronounced enrichment of Ni relative to Fe and Sn, confirming the formation of a Ni-rich ternary alloy with reduced incorporation of the latter elements. These findings suggest that increasing the cathodic overpotential favors preferential Ni deposition while suppressing the co-deposition of Fe and Sn species, thereby modifying the alloy composition and consequently influencing the surface structure and electrochemical properties of the catalyst.

To further confirm this observation, the composition ratio value (CRV), defined as the ratio of the metal mass fraction in the deposit to that in the electrolyte was determined using equation (1) [26].

$$CRV = \frac{Mass\ fraction\ of\ metal\ in\ deposits\ (\%wt)}{Mass\ fraction\ of\ metal\ in\ electrolyte\ (\%wt)} \quad (1)$$

Where M = Co and Ni.

The calculated CRV values for NiFeSn(A) were 0.75, 1.60, and 1.76 for Ni, Fe, and Sn, respectively, whereas NiFeSn(B) exhibited CRV values of 0.87, 1.44, and 1.06. These results indicate that Ni deposition is relatively suppressed compared with its electrolyte concentration (CRV < 1), while Fe and Sn are preferentially incorporated into the deposits (CRV > 1), confirming the occurrence of anomalous ternary co-deposition behavior [27]. Notably, NiFeSn(A) exhibits substantially greater Fe and Sn enrichment, particularly for Sn incorporation, implying that the lower deposition potential favors simultaneous co-reduction and stabilization of Fe and Sn species within the alloy. Conversely, NiFeSn(B) accelerates Ni reduction kinetics, thereby limiting Fe and Sn incorporation and producing a Ni-enriched deposit.

The electrochemical behavior of the NiFeSn electrocatalysts toward ethanol oxidation was further analyzed by comparing the voltammetric response in 1 M KOH with and without ethanol, as shown in Fig. 2(a). In the absence of ethanol, both NiFeSn(A) and NiFeSn(B) exhibit a characteristic anodic redox feature centered at approximately 0.55–0.65 V vs Ag/AgCl, corresponding to the reversible transformation of $Ni(OH)_2$ to NiOOH during the forward scan and its subsequent reduction during the reverse scan [28]. The electrochemical oxidation of nickel species in alkaline electrolyte can be represented by the following reactions:

$$Ni + 2OH^- \rightarrow NiOH_2 + 2e \quad (2)$$

$$Ni(OH)_2 + OH^- \leftrightarrow NiOOH + H_2O + e \quad (3)$$

At lower anodic potentials, metallic Ni is initially converted into $NiOH_2$ followed by its oxidation into electroactive NiOOH. The anodic peak corresponds to the formation of NiOOH, while the cathodic peak is associated with the reduction of NiOOH back to $Ni(OH)_2$. The formation of NiOOH is particularly important because it acts as the active oxidizing species responsible for ethanol electrooxidation in alkaline media.

Upon the addition of ethanol, a pronounced increase in anodic current density is observed, accompanied by the appearance of two distinct oxidation peaks, confirming the electrocatalytic oxidation of ethanol mediated by surface nickel oxyhydroxide species. Ethanol oxidation becomes significant near the potential region of NiOOH formation, indicating that the generated NiOOH species serve as active sites for ethanol electrooxidation through a redox-mediated mechanism. In the forward scan, the anodic current is attributed to the oxidation of freshly adsorbed ethanol species on the catalyst surface, whereas the anodic peak observed in the reverse scan is related to the oxidation of residual incompletely oxidized carbonaceous intermediates formed during the forward sweep [29]. For NiFeSn(A), this forward oxidation peak appears at 838 mV with a peak current of 104.44 mA, whereas NiFeSn(B) exhibits a lower peak potential of 753 mV and a lower peak current of 63.17 mA. The substantially higher forward peak current of NiFeSn(A) indicates superior electrocatalytic activity toward ethanol oxidation, which can be associated with its more favorable surface composition and morphology, providing a larger number of accessible active sites for ethanol adsorption and oxidation. Although NiFeSn(B) shows ethanol oxidation at a lower potential, the lower oxidation current suggests comparatively reduced catalytic efficiency.

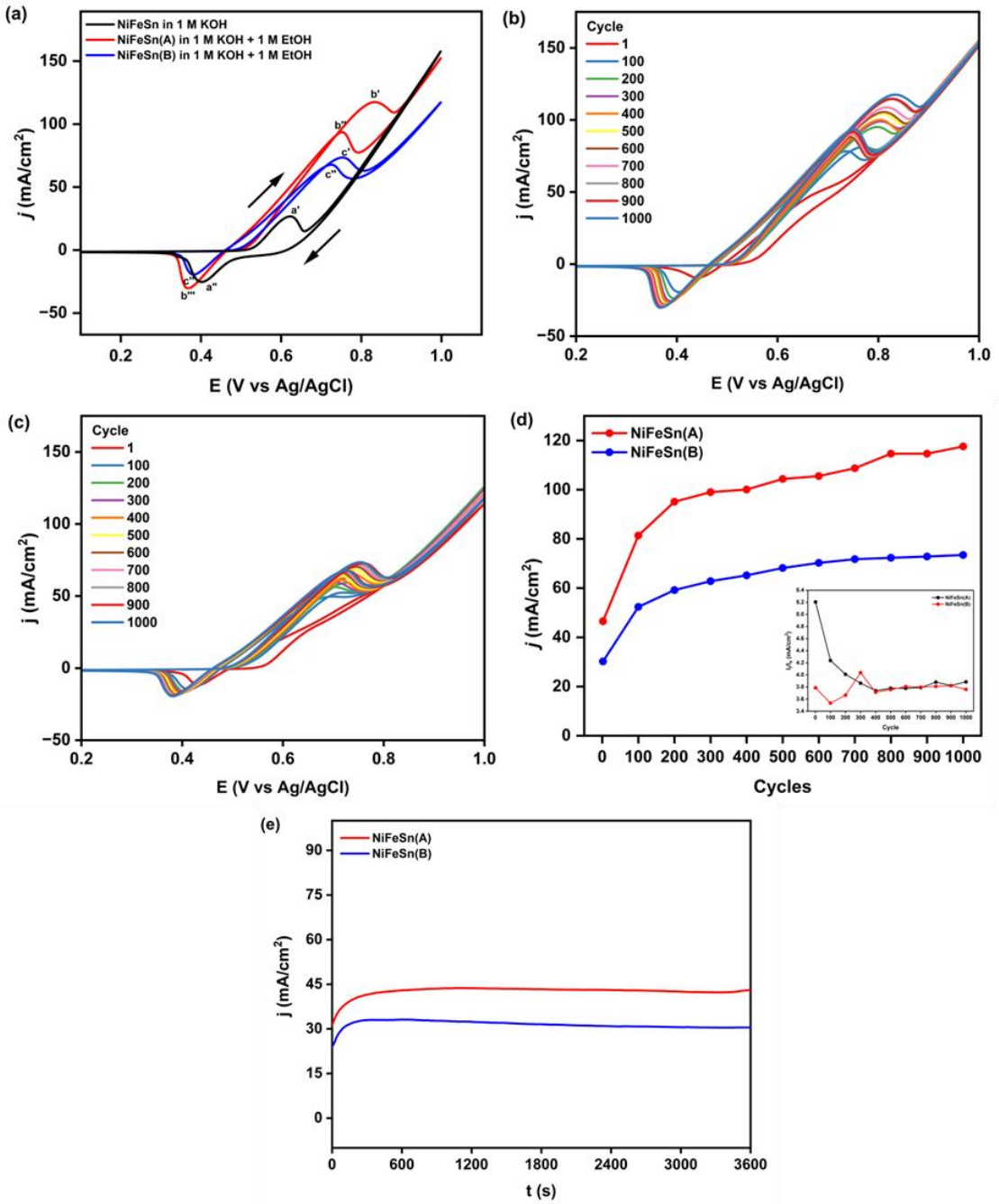

Figure 2. (a) Cyclic voltammograms of NiFeSn in 1 M KOH and NiFeSn(A) and NiFeSn(B) in 1 M KOH + 1 M ethanol, (b,c) Evolution of cyclic voltammograms for NiFeSn(A) and NiFeSn(B), respectively, recorded over 1000 consecutive cycles, demonstrating the changes in electrochemical activity during prolonged cycling. (d) Variation of forward peak current density (j_p) as a function of cycle number for NiFeSn(A) and NiFeSn(B), (e) Chronoamperometric responses of NiFeSn(A) and NiFeSn(B) measured for 3600 s

Simultaneously, the reduction peak intensity in the reverse scan decreases compared to that in ethanol-free electrolyte, suggesting the consumption of NiOOH species through chemical interaction with ethanol molecules. This phenomenon indicates that ethanol oxidation proceeds via a mediated electrocatalytic mechanism involving the continuous regeneration of NiOOH active species. The catalytic oxidation mechanism can be represented as [30]:

$$NiOOH + Ethanol \rightarrow Ni(OH)_2 + products \quad (4)$$

During the reverse scan, a cathodic peak emerges at lower potentials, centered at 368 and 382 mV for NiFeSn(A) and NiFeSn(B), respectively, with corresponding peak currents of 26.91 and 16.79 mA. Compared to the ethanol-free electrolyte, the cathodic reduction peak of NiOOH becomes less pronounced in the presence of ethanol, indicating the consumption of NiOOH species through chemical interaction with ethanol molecules. This behavior confirms that ethanol oxidation proceeds via a mediated

electrocatalytic pathway in which NiOOH species are continuously generated electrochemically and subsequently consumed during ethanol oxidation, followed by regeneration throughout the voltammetric cycle.

A comparison between the two electrocatalysts reveals that NiFeSn(A) exhibited superior electrochemical performance compared to NiFeSn(B). The forward peak current density (j/mA cm^{-2}), calculated by normalizing the observed current to the geometric area of the electrocatalyst (mA cm^{-2}), is a key parameter for evaluating EOR activity and extracted at the peak potential from the CV curves. As illustrated in Fig. 2(a), the forward anodic current of NiFeSn(A) increased continuously over an extended potential range, eventually reaching a peak current density (j_p) of 117.61 mA cm^{-2}, 1.60 times higher than NiFeSn(B) that only 73.47 mA cm^{-2}. Specifically, NiFeSn(A) showed a lower onset potential (E_{op}) of 570 mV compared with 579 mV for NiFeSn(B), indicating more favorable reaction kinetics and easier initiation of ethanol oxidation. A more negative onset potential indicates enhanced catalytic activity and reduced overpotential, reflecting more favorable ethanol oxidation kinetics [31].

The broader anodic response observed for NiFeSn(A) during the positive-going scan may be attributed to the progressive formation of reactive surface intermediates and the enhanced availability of adsorbed hydroxyl species (OH_{ads}), which facilitate the oxidative removal of poisoning carbonaceous intermediates generated during ethanol electro-oxidation [32]. The presence of OH_{ads} species plays a critical role in promoting the oxidation of strongly adsorbed intermediates, thereby regenerating catalytically active sites and sustaining the ethanol oxidation process [33]. This interpretation is further supported by the higher I_f/I_b ratio obtained for NiFeSn(A) (3.88) compared to NiFeSn(B) (3.76), indicating superior tolerance toward poisoning intermediates and more efficient recovery of active catalytic sites during ethanol electro-oxidation [34]. Consequently, the superior electrocatalytic performance of NiFeSn(A) can be attributed to its enhanced ethanol oxidation kinetics, improved utilization of electrochemically active sites, and greater resistance against surface poisoning.

Table 2. Electrocatalytic parameters of NiFeSn towards EOR.

Sample	Forward Scan		Backward Scan		E_{op} (mV)	j_p (mA/cm^2)	I_f/I_b
	E_p (mV)	I_p (mA)	E_p (mV)	I_p (mA)			
NiFeSn(A)	838	104.44	368	26.91	570	117,61	3.88
NiFeSn(B)	753	63.17	382	16.79	579	73,47	3.76

Since tolerance toward poisoning intermediates is closely associated with catalyst durability during prolonged electrochemical operation, the stability of the as-prepared catalysts was further systematically evaluated. In ethanol electro-oxidation, the continuous accumulation of adsorbed carbonaceous species, particularly CO-like intermediates and acetate-related fragments, can progressively block active sites and deteriorate catalytic activity over time. To verify this correlation, the durability of the NiFeSn electrocatalysts was investigated through repeated cyclic voltammetry (CV) for 1000 cycles and chronoamperometric (CA) measurements conducted for 3600 s in alkaline electrolyte.

As shown in Fig. 2d, the evolution of the forward oxidation peak current density (j_p), corresponding to ethanol electro-oxidation, was monitored as a function of cycle number to evaluate the electrochemical durability and activation behavior of the catalysts during prolonged operation. Interestingly, both catalysts exhibited a progressive increase in anodic peak current density with increasing cycle number, suggesting a gradual electrochemical activation process rather than catalyst deactivation. This enhancement may be attributed to surface reconstruction and the progressive formation of electrochemically active oxyhydroxide species during repetitive cycling, which facilitate ethanol adsorption and accelerate oxidation kinetics, while continuous cycling may also improve electrolyte penetration and accessibility of catalytically active sites [17]. Notably, NiFeSn(A) consistently delivered substantially higher current density throughout the durability test, increasing from approximately 46.5 to 117.5 mA cm^{-2} after 1000 cycles, whereas NiFeSn(B) increased from around 30.1 to 73.4 mA cm^{-2}, indicating a more favorable activation process and superior preservation of catalytic activity for NiFeSn(A). Further insight into catalyst tolerance toward poisoning intermediates is provided by the evolution I_f/I_b, shown in the inset of Fig. 2d. Initially, NiFeSn(A) exhibited a higher value than NiFeSn(B), indicating more efficient ethanol oxidation during the forward scan and lower accumulation of incompletely oxidized intermediates on the catalyst surface. However, with increasing cycle number, the If/Ib ratio of NiFeSn(A) gradually decreased and stabilized, whereas that of NiFeSn(B) slightly increased, resulting in comparable values after prolonged cycling, suggesting that repeated electrochemical cycling promotes surface stabilization and establishes a steady-state adsorption–

oxidation equilibrium for both catalysts. Nevertheless, despite the convergence in I_f/I_b values at extended cycling, NiFeSn(A) maintained markedly higher anodic current density, indicating that its superior catalytic activity is preserved while exhibiting comparable resistance toward poisoning intermediates.

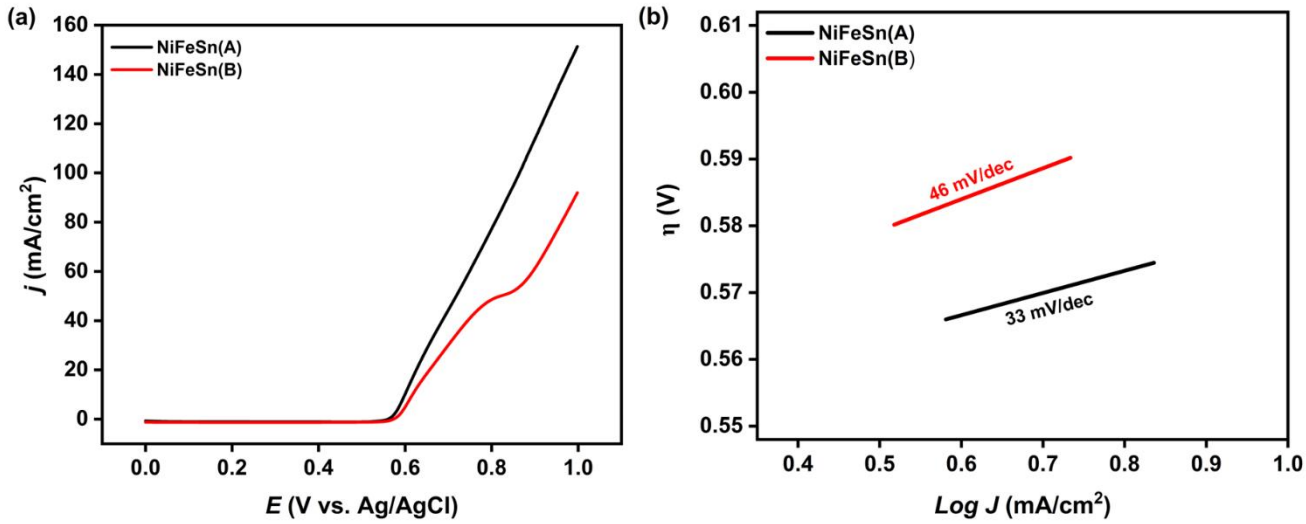

Figure 3. (a) LSV curves and (b) Tafel slope of NiFeSn catalyst in 1 M KOH containing 1 M EtOH.

To further evaluate long-term catalytic stability, chronoamperometric (CA) measurements were conducted in the same electrolyte solution at 0.65 V vs Ag/AgCl shown in Fig. 2e. Both catalysts exhibited a characteristic current–time profile consisting of an initial rapid increase in current density followed by a quasi-steady-state region during prolonged electrolysis. The initial increase in current density can be attributed to the progressive electrochemical activation of the catalyst surface, accompanied by enhanced ethanol adsorption and dehydrogenation processes. Subsequently, the current density approached a relatively stable plateau, indicating the establishment of a dynamic balance between ethanol oxidation kinetics and the accumulation/removal of adsorbed reaction intermediates.

A distinct difference in catalytic stability was observed between the two catalysts. NiFeSn(A) consistently delivered a higher current density throughout the entire electrolysis period, stabilizing at approximately 43–45 mA cm^{-2} after the initial activation stage, whereas NiFeSn(B) reached a lower steady-state current density of approximately 30–32 mA cm^{-2}. More importantly, NiFeSn(A) exhibited only a marginal decrease in current density over time, indicating minimal catalyst deactivation and superior resistance toward poisoning intermediates. In contrast, NiFeSn(B) displayed a more pronounced gradual current decay, suggesting a greater extent of active-site blockage by adsorbed carbonaceous species. The higher residual current density retained by NiFeSn(A) after 3600 s confirms its stronger anti-poisoning capability and improved long-term operational stability during ethanol electro-oxidation. Furthermore, the poisoning rate (δ) of the NiFeSn catalysts was determined using the following equation [35]:

$$\delta = \frac{1000}{I_0} \times \left(\frac{dI}{dt}\right)_{t \geq 500\ s} \quad (5)$$

where I_o represents the current at the y-intercept and *(dI/dt)* corresponds to the slope obtained from the linear regression of the chronoamperometric curve after 500 s. The calculated poisoning rates were $\delta \approx -0.011$ %·s^{-1} for NiFeSn(A) and $\delta \approx -0.034$ %·s^{-1} for NiFeSn(B), indicating that the current decay of NiFeSn(B) proceeded roughly three times faster than that of NiFeSn(A).

The electrocatalytic kinetics of the prepared NiFeSn electrocatalysts toward the ethanol oxidation reaction (EOR) were further investigated by Tafel polarization analysis. Linear sweep voltammetry (LSV) measurements were performed at a low scan rate of 10 mV s^{-1} to minimize capacitive contributions and provide a reliable evaluation of the reaction kinetics. The kinetic parameters were determined from the linear relationship between the electrode potential (E vs. Ag/AgCl) and the logarithm of the current density (log j), as shown in Fig. 3(b). The Tafel behavior follows the classical Tafel equation [36]:

$$b = \frac{2.303RT}{\alpha nF} \quad (6)$$

where (R) is the universal gas constant, (T) is the absolute temperature, (F) is the Faraday constant, (\alpha) is the charge-transfer coefficient, and (n) is the number of electrons involved in the rate-determining step. The Tafel slope (b) was obtained from the linear region of the polarization curves by linear regression and serves as an indicator of the charge-transfer kinetics during ethanol

oxidation. The calculated Tafel slopes for NiFeSn(A) and NiFeSn(B) were 33.26 and 46.26 mV dec^{-1}, respectively. The lower Tafel slope of NiFeSn(A) indicates more favorable reaction kinetics, requiring a smaller increase in overpotential to achieve a corresponding increase in current density. Using the experimentally obtained Tafel slopes, the values of the kinetic parameter (αn) were calculated to be 1.78 for NiFeSn(A) and 1.28 for NiFeSn(B). Although (α) and (n) cannot be independently determined from Tafel analysis alone, the larger (αn) value of NiFeSn(A) suggests more efficient interfacial charge transfer and a lower kinetic barrier for ethanol oxidation. These findings are consistent with the EIS results, where NiFeSn(A) exhibited a lower charge-transfer resistance, confirming its superior electrocatalytic kinetics toward the EOR [37].

Using the experimentally obtained Tafel slopes, the values of αn are 1.78 for NiFeSn(A) and 1.28 for NiFeSn(B). Although the individual values of the charge-transfer coefficient (α) and the number of electrons involved in the rate-determining step (n) cannot be determined independently from Tafel analysis alone, the larger αn\alpha nαn value of NiFeSn(A) indicates more favorable charge-transfer kinetics during ethanol oxidation. This result is consistent with its lower Tafel slope (33.26 mV dec^{-1}), meaning that a smaller increase in overpotential is required to achieve a given increase in current density. In contrast, the lower αn value of NiFeSn(B) reflects slower interfacial electron-transfer kinetics and a higher kinetic barrier for the reaction.

intermediates, whereas Fe modifies the electronic structure of Ni active sites, thereby enhancing electron transfer and accelerating the reaction kinetics [32]. Consequently, the lower Tafel slope exhibited by NiFeSn(A) reflects a more efficient charge-transfer process at the electrode–electrolyte interface, which is in good agreement with its superior electrocatalytic performance observed from CV and CA measurements.

To further elucidate the interfacial charge-transfer characteristics, EIS measurements were conducted under EOR conditions over a frequency range of 10^{-1}–10^{5} Hz. The corresponding Nyquist plots are presented in Fig. 5, while the inset illustrates the equivalent electrical circuit used for fitting. Prior to electrochemical cycling, NiFeSn(A) and NiFeSn(B) exhibited R_s values of 1.591 ± 0.036 Ω·cm² and 1.594 ± 0.027 Ω·cm², respectively. After CV cycling, the R_s values slightly increased to 1.710 ± 0.027 Ω·cm² for NiFeSn(A) and 2.120 ± 0.044 Ω·cm² for NiFeSn(B). A low Rs reflects lower ohmic resistance and improved electrode–electrolyte contact, which facilitates charge transport and contributes to the decrease in R_{ct} [38]. The relatively small variation in R_s suggests that the overall conductivity of the electrolyte system remained stable during electrochemical operation and that the observed performance differences mainly originated from interfacial charge-transfer processes rather than bulk solution resistance.

A more significant distinction between the catalysts is evident from the charge-transfer resistance (R_{ct}), which

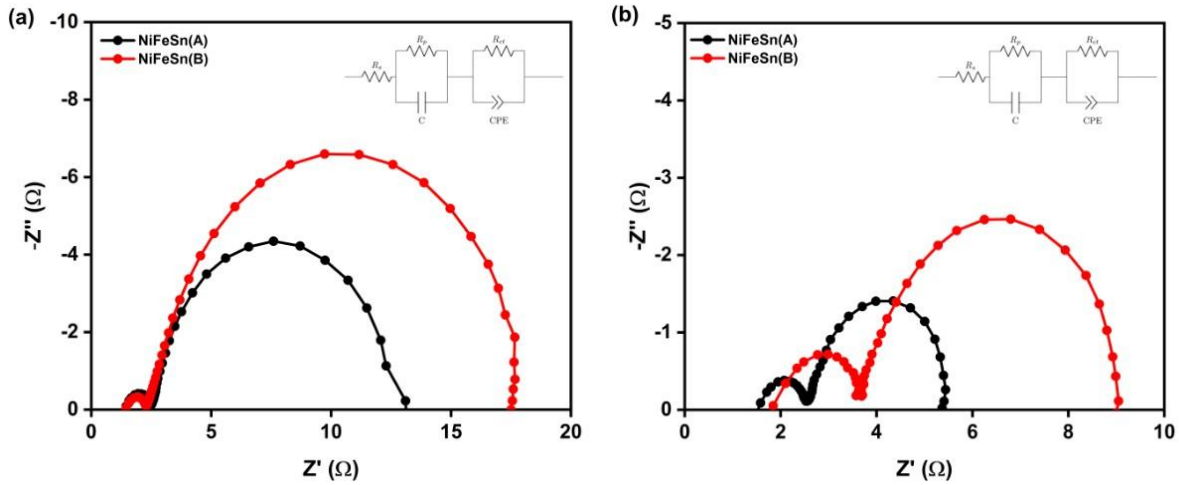

Figure 4. Nyquist plot of NiFeSn (a) before and (b) after CV measurement.

The superior kinetic behavior of NiFeSn(A) can be attributed to the synergistic interaction among Ni, Fe, and Sn species, which collectively promote ethanol oxidation through both electronic and bifunctional effects. Specifically, the incorporation of Sn facilitates the formation of surface hydroxyl species (OH_{ads}), which assist in the oxidative removal of poisoning carbonaceous

reflects the ease of electron transfer across the electrode–electrolyte interface during ethanol electrooxidation. Before cycling, NiFeSn(A) exhibited a substantially lower R_{ct} value (9.897 ± 0.243 Ω·cm²) compared to NiFeSn(B) (16.416 ± 0.264 Ω·cm²), indicating enhanced interfacial conductivity and more efficient electron transfer during EOR [39]. After electrochemical activation through CV

cycling, both catalysts experienced a pronounced decrease in R_{ct}, reaching 2.933 ± 0.071 Ω·cm² for NiFeSn(A) and 5.470 ± 0.152 Ω·cm² for NiFeSn(B). The reduction in R_{ct} after cycling suggests activation of the catalyst surface through structural rearrangement and progressive exposure of catalytically accessible sites. The fitted EIS parameters for all samples before and after electrochemical cycling are summarized in Table 3.

The electrocatalytic performance is strongly influenced by the number of electrochemically accessible active sites and the charge-transfer efficiency at the electrode–electrolyte interface. To assess the density of electrochemically accessible active sites, the electrochemically active surface area (*ECSA*) of the NiFeSn catallyst was estimated from the electrochemical double-layer capacitance (C_{dl}) derived from electrochemical impedance spectroscopy (EIS). Since C_{dl} is proportional to the effective interfacial area, it provides a reliable measure of the active surface area available for the ethanol oxidation reaction (EOR). The C_{dl} values were calculated from the constant phase element parameters obtained from EIS fitting according to Equation (7) [40]:

$$C_{dl} = Y_{dl}^{\frac{1}{n}} \left(\frac{1}{R_s} + \frac{1}{R_{ct}}\right)^{\frac{n-1}{n}} \quad (7)$$

Subsequently, the *ECSA* was determined using the following equation (8):

$$ECSA = \frac{C_{dl}}{C_s} \quad (8)$$

where C_s is the specific capacitance using an average value of 0.040 mF cm^{-2} referred to literature reports [41].

Prior to electrochemical cycling, NiFeSn(A) exhibited a higher double-layer capacitance (C_{dl}) of 3.067 mF than NiFeSn(B) (1.152 mF), indicating a larger electrochemically active interface. This observation is consistent with the higher electrochemically active surface area (*ECSA*) of NiFeSn(A), which reached 76.68 cm², compared with 28.80 cm² for NiFeSn(B). The larger C_{dl} and *ECSA* values suggest that NiFeSn(A) possesses a greater density of electrochemically accessible active sites, thereby facilitating ethanol oxidation [42]. After CV cycling, the C_{dl} values increased to 3.539 mF for NiFeSn(A) and 2.355 mF for NiFeSn(B), while the *ECSA* values increased to 88.48 cm² and 58.88 cm², respectively. The increase in ECSA after cycling suggests the exposure of additional active sites and improved electrolyte accessibility, particularly for NiFeSn(A).

The roughness factor (*RF*), calculated from the ratio of *ECSA* to the geometric electrode area, further confirms the superior surface characteristics of NiFeSn(A). The *RF* values increased from 86.25 before cycling to 99.53 after cycling, whereas NiFeSn(B) exhibited lower values of 33.49 and 68.47, respectively. The consistently higher *RF* of NiFeSn(A) indicates a more electrochemically textured surface with a larger population of accessible active sites, which enhances reactant accessibility and contributes to its superior electrocatalytic performance toward ethanol oxidation [43].

Table 3. The fitted EIS parameters of NiFeSn catalyst.

Parameters	Before CV		After CV	
	NiFeSn(A)	NiFeSn(B)	NiFeSn(A)	NiFeSn(B)
Rs (Ω·cm²)	1.591 ± 0.036	1.594 ± 0.027	1.710 ± 0.027	2.120 ± 0.044
Rp (Ω·cm²)	0.947 ± 0.038	0.725 ± 0.028	0.857 ± 0.028	1.547 ± 0.046
C (μF)	7.55 ± 0.73	9.86 ± 0.91	7.87 ± 0.61	3.51 ± 0.25
CPE-T (mF·cm^{-2})	4.594 ± 0.274	3.527 ± 0.134	4.654 ± 0.438	3.768 ± 0.372
CPE-P (n)	0.936 ± 0.014	0.850 ± 0.008	0.956 ± 0.019	0.924 ± 0.021
Rct (Ω·cm²)	9.897 ± 0.243	16.416 ± 0.264	2.933 ± 0.071	5.470 ± 0.152
C_{dl} (mF)	3.067	1.152	3.539	2.355
ECSA (cm^2)	76.68	28.80	88.48	58.88
RF	86.25	33.49	99.53	68.47

The superior ethanol electrooxidation performance of NiFeSn(A) can be attributed to the synergistic effects of its composition and surface morphology. Cyclic voltammetry measurements revealed that NiFeSn(A) delivered a higher anodic peak current density (117.61 mA cm^{-2}) and a slightly lower onset potential (570 mV) than NiFeSn(B) (73.47 mA cm^{-2} and 579 mV), indicating more favorable ethanol oxidation kinetics. Elemental analysis based on atomic percentage (at.%) showed that NiFeSn(A) contains higher Fe (35.40 at.%) and Sn (7.15 at.%) contents than NiFeSn(B) (31.01 at.% Fe and 4.22 at.% Sn), resulting in lower Ni/Fe and Ni/Sn ratios (1.62 and 8.03 for NiFeSn(A) vs. 2.09 and 15.35 for NiFeSn(B). The increased Fe content can modulate the electronic structure of Ni active sites and facilitate electron transfer, while the higher Sn content promotes the formation of OH_{ads} species that assist in the oxidative removal of poisoning carbonaceous intermediates. These electronic and bifunctional effects

collectively accelerate the reaction kinetics and enhance catalyst utilization [44].

Table 4. Comparison of trimetallic catalyst performance toward the ethanol electrooxidation reaction.

Electrocatalyst	Electrolyte	Current density	Reference
Ni-Fe-Sn	1 M KOH + 1 M EtOH	117,61 mA.cm²	This study
Co-Ni-Mo	0.5 M NaOH + 1 M EtOH	24.9 mA.cm²	[45]
Cu-Pt-Pd	1 M KOH + 1 M EtOH	166.7 mA.cm²	[46]
Pt-Ir-Ni	1 M KOH + 1 M EtOH	116.7 mA.cm²	[47]
Pt-Sn-Ni	1 M NaOH + 1 M EtOH	117.25 mA.cm²	[48]
Pd-Pt-Au	1 M KOH + 1 M EtOH	32.45 mA.cm²	[49]

Moreover, SEM observations revealed that NiFeSn(A) consists of densely packed and uniformly distributed quasi-spherical particles that form a rough and interconnected architecture. Such a morphology provides a larger electrochemically accessible surface area and facilitates electrolyte penetration and charge transport, as evidenced by its higher C_{dl}, *ECSA*, and roughness factor (*RF*), together with a lower charge-transfer resistance (R_{ct}). Consequently, NiFeSn(A) exhibited a slightly higher I_f/I_b ratio (3.88) than NiFeSn(B) (3.76), indicating improved tolerance toward poisoning intermediates and enhanced catalytic stability. In contrast, the lower Fe and Sn contents and the more compact, partially agglomerated morphology of NiFeSn(B) likely limit active-site exposure and hinder charge transfer, resulting in inferior electrocatalytic performance. Overall, these results demonstrate that the synergistic interplay between composition and interconnected granular morphology is crucial for enhancing the activity, kinetics, and stability of NiFeSn(A) toward the ethanol oxidation reaction. Furthermore, as summarized in Table 4, NiFeSn(A) outperforms or is comparable to many previously reported electrocatalysts in terms of current density.

4. Conclusion

This study demonstrates that the electrocatalytic performance of Ni–Fe–Sn catalysts toward the ethanol oxidation reaction is strongly dependent on surface morphology. The densely packed granular architecture of NiFeSn(A) provided a more favorable electrochemical environment than the sparse agglomerated morphology of NiFeSn(B), resulting in enhanced catalytic activity, faster charge-transfer kinetics, and improved stability. The superior performance of NiFeSn(A) is attributed to its higher electrochemically accessible surface area, greater active-site utilization, and enhanced resistance to intermediate poisoning, which collectively facilitate ethanol oxidation. These findings establish a clear morphology–activity relationship and highlight the importance of morphology engineering through potentiostatic electrodeposition as an effective strategy for developing high-performance Ni-based electrocatalysts for direct ethanol fuel cells.

Author contributions

Juliandi Siregar: Conceptualization, Methodology, Investigation, Formal analysis, Data curation, Writing – original draft, Visualization. **Muhammad Fathar Aulia:** Conceptualization, Supervision, Validation, Resources, Writing – review & editing, Project administration.

Conflicts of interest

There are no conflicts to declare.

Acknowledgement

The authors gratefully acknowledge to the Center for Science Innovation for providing the research facilities and support necessary to conduct this study.

References

[1] F.S. Saleh, E.B. Easton, Assessment of the ethanol oxidation activity and durability of Pt catalysts with or without a carbon support using Electrochemical Impedance Spectroscopy, *J. Power Sources*. **246** (2014) 392–401. https://doi.org/10.1016/j.jpowsour.2013.07.109.

[2] F.P. Lohmann-Richters, B. Abel, Á. Varga, In situ determination of the electrochemically active platinum surface area: Key to improvement of solid acid fuel cells, *J. Mater. Chem. A*. **6** (2018) 2700–2707. https://doi.org/10.1039/c7ta10110d.

[3] S. Li, Y. Wang, Y. Li, X. Fang, Y. Liu, M. Li, Z. Wang, Y. Gao, H. Sun, F. Gao, X. Zhang, X. Dai, PtNiCu nanowires with advantageous lattice-plane boundary for enhanced ethanol electrooxidation, *Nano Res.* **15** (2022) 2877–2886. https://doi.org/10.1007/s12274-021-3881-2.

[4] P. Bishnoi, K. Mishra, S.S. Siwal, V.K. Gupta, V.K. Thakur, Direct Ethanol Fuel Cell for Clean Electric Energy: Unravelling the Role of Electrode Materials for a Sustainable Future, *Adv. Energy Sustain. Res.* **5** (2024). https://doi.org/10.1002/aesr.202300266.

[5] J. Zhan, M. Cai, C. Zhang, C. Wang, Synthesis of mesoporous NiCo2O4 fibers and their electrocatalytic activity on direct oxidation of ethanol in alkaline media, *Electrochim. Acta*. **154** (2015) 70–76. https://doi.org/10.1016/j.electacta.2014.12.078.

[6] J. Piwowar, A. Lewera, On the absence of a beneficial role of Rh towards C[sbnd]C bond cleavage during low temperature ethanol electrooxidation on PtRh nanoalloys, *J. Electroanal. Chem.* **875** (2020) 114229. https://doi.org/10.1016/j.jelechem.2020.114229.

[7] D. Rohendi, A. Rachmat, N. Syarif, Fabrication and Characterization of Pt-Co/C Catalyst for Fuel Cell Electrode, in: J. Phys. Conf. Ser., Institute of Physics Publishing, 2018. https://doi.org/10.1088/1742-6596/1095/1/012007.

[8] M. Mayilvel Dinesh, T. Huang, S. Yao, G. Sun, S. Mao, Hafnium sulphide-carbon nanotube composite as Pt support and active site-enriched catalyst for high performance methanol and ethanol oxidations in alkaline electrolytes, *J. Power Sources*. **410–411** (2019) 204–212. https://doi.org/10.1016/j.jpowsour.2018.11.021.

[9] S. Xiang, L. Wang, C.C. Huang, Y.J. Fan, H.G. Tang, L. Wei, S.G. Sun, Concave cubic PtLa alloy nanocrystals with high-index facets: Controllable synthesis in deep eutectic solvents and their superior electrocatalytic properties for ethanol oxidation, *J. Power Sources*. **399** (2018) 422–428. https://doi.org/10.1016/j.jpowsour.2018.07.102.

[10] L. Wang, W. Wu, Z. Lei, T. Zeng, Y. Tan, N. Cheng, X. Sun, High-performance alcohol electrooxidation on Pt3Sn-SnO2 nanocatalysts synthesized through the transformation of Pt-Sn nanoparticles, *J. Mater. Chem. A*. **8** (2020) 592–598. https://doi.org/10.1039/c9ta10886f.

[11] A.N. Golikand, M. Asgari, M.G. Maragheh, S. Shahrokhian, Methanol electrooxidation on a nickel electrode modified by nickel-dimethylglyoxime complex formed by electrochemical synthesis, *J. Electroanal. Chem.* **588** (2006) 155–160. https://doi.org/10.1016/j.jelechem.2005.11.033.

[12] Z. Angeles-Olvera, A. Crespo-Yapur, O. Rodríguez, J. Cholula-Díaz, L. Martínez, M. Videa, Nickel-Based Electrocatalysts for Water Electrolysis, *Energies*. **15** (2022) 1609. https://doi.org/10.3390/en15051609.

[13] Y. Zhang, L. Zhang, C. Song, Y. Qin, L. Lu, W. Zhu, Z. Zhuang, Nickel chalcogenides as selective ethanol oxidation electro-catalysts and their structure–performance relationships, *Chem. Commun.* **58** (2022) 2496–2499. https://doi.org/10.1039/D1CC07086J.

[14] Z. Miao, C. Xu, J. Zhan, Z. Xu, Morphology-control and template-free fabrication of bimetallic Cu–Ni alloy rods for ethanol electro-oxidation in alkaline media, *J. Alloys Compd.* **855** (2021). https://doi.org/10.1016/j.jallcom.2020.157438.

[15] S.A. Theofanidis, R. Batchu, V. V. Galvita, H. Poelman, G.B. Marin, Carbon gasification from Fe-Ni catalysts after methane dry reforming, *Appl. Catal. B Environ.* **185** (2016) 42–55. https://doi.org/10.1016/j.apcatb.2015.12.006.

[16] D. González-Flores, K. Klingan, P. Chernev, S. Loos, M.R. Mohammadi, C. Pasquini, P. Kubella, I. Zaharieva, R.D.L. Smith, H. Dau, Nickel-iron catalysts for electrochemical water oxidation-redox synergism investigated by: In situ X-ray spectroscopy with millisecond time resolution, *Sustain. Energy Fuels*. **2** (2018) 1986–1994. https://doi.org/10.1039/c8se00114f.

[17] D. Martín-Yerga, G. Henriksson, A. Cornell, Effects of Incorporated Iron or Cobalt on the Ethanol Oxidation Activity of Nickel (Oxy)Hydroxides in Alkaline Media, *Electrocatalysis*. **10** (2019) 489–498. https://doi.org/10.1007/s12678-019-00531-8.

[18] J.-Q. Lian, Y.-H. Wu, H.-A. Zhang, S.-Y. Gu, Y. Chen, J.-D. Ma, Y.-L. Hu, One-step electrodeposition synthesis of a ni–fe–sn electrode for hydrogen production in alkaline solution, *Mater. Lett.* **227** (2018) 124–127. https://doi.org/10.1016/j.matlet.2018.05.050.

[19] M. Gao, X. Zhang, S. Dai, K.-W. Wang, Tin as a co-catalyst for electrocatalytic oxidation and reduction reactions, *Inorg. Chem. Front.* **11** (2024) 1019–1047. https://doi.org/10.1039/D3QI02010J.

[20] M. Taei, E. Havakeshian, H. Salavati, F. Abedi, Electrocatalytic oxidation of ethanol on a glassy carbon electrode modified with a gold nanoparticle-coated hydrolyzed CaFe-Cl layered double hydroxide in alkaline medium, *RSC Adv.* **6** (2016) 27293–27300. https://doi.org/10.1039/c5ra20915c.

[21] A. Pei, G. Zheng, F. Shi, Y. Li, Y. Cui, Nanoscale Nucleation and Growth of Electrodeposited Lithium Metal, *Nano Lett.* (2017). https://doi.org/10.1021/acs.nanolett.6b04755.

[22] J. Lin, M. Kilani, M. Baharfar, R. Wang, G. Mao, Understanding the nanoscale phenomena of nucleation and crystal growth in electrodeposition, *Nanoscale*. (2024). https://doi.org/10.1039/d4nr02389g.

[23] X. Tan, S. Chen, D. Yan, R. Du, Q. Zhong, L. Liao, Z. Tang, F. Zeng, Recent advances in Ni-based catalysts for the

electrochemical oxidation of ethanol, *J. Energy Chem.* **98** (2024) 588–614. https://doi.org/10.1016/J.JECHEM.2024.06.045.

[24] Y. Wu, Y. Zhang, Y. Wang, Z. He, Z. Gu, S. You, Potentiostatic electrodeposited of Ni–Fe–Sn on Ni foam served as an excellent electrocatalyst for hydrogen evolution reaction, *Int. J. Hydrogen Energy*. **46** (2021) 26930–26939. https://doi.org/10.1016/j.ijhydene.2021.05.189.

[25] J. Zhou, X. Meng, P. Ouyang, R. Zhang, H. Liu, C. Xu, Z. Liu, Electrochemical behavior and electrodeposition of Fe-Co-Ni thin films in choline chloride/urea deep eutectic solvent, *J. Electroanal. Chem.* **919** (2022). https://doi.org/10.1016/j.jelechem.2022.116516.

[26] A. Ayuningsih, Potentiostatic Electrodeposition of FeCo Thin Films : Influence of Deposition Temperature and Saccharin Concentration, **4** (2025) 50–57.

[27] S. Budi, A. Manaf, The effects of saccharin on the electrodeposition of NiCoFe films on a flexible substrate, *Mater. Res. Express*. **8** (2021). https://doi.org/10.1088/2053-1591/ac1a2c.

[28] D.A. Links, Preparation of graphene supported nickel nanoparticles and their application to methanol electrooxidation in alkaline medium w, (2012) 1108–1113. https://doi.org/10.1039/c2nj20690k.

[29] Q. Zhang, T. Chen, R. Jiang, F. Jiang, Comparison of electrocatalytic activity of Pt1-: XPdx/C catalysts for ethanol electro-oxidation in acidic and alkaline media, *RSC Adv.* **10** (2020) 10134–10143. https://doi.org/10.1039/d0ra00483a.

[30] L. Yaqoob, T. Noor, N. Iqbal, A comprehensive and critical review of the recent progress in electrocatalysts for the ethanol oxidation reaction, *RSC Adv.* **11** (2021) 16768–16804. https://doi.org/10.1039/d1ra01841h.

[31] Y. Hou, H. Yuan, Z. Wen, S. Cui, X. Guo, Z. He, J. Chen, Nitrogen-doped graphene/CoNi alloy encased within bamboo-like carbon nanotube hybrids as cathode catalysts in microbial fuel cells, *J. Power Sources*. **307** (2016) 561–568. https://doi.org/10.1016/j.jpowsour.2016.01.018.

[32] J. Datta, A. Dutta, S. Mukherjee, The beneficial role of the cometals Pd and Au in the carbon-supported PtPdAu catalyst toward promoting ethanol oxidation kinetics in alkaline fuel cells: Temperature effect and reaction mechanism, *J. Phys. Chem. C*. **115** (2011) 15324–15334. https://doi.org/10.1021/jp200318m.

[33] M.L. Yola, T. Eren, N. Atar, H. Saral, I. Ermiş, Direct-methanol Fuel Cell Based on Functionalized Graphene Oxide with Mono-metallic and Bi-metallic Nanoparticles: Electrochemical Performances of Nanomaterials for Methanol Oxidation, *Electroanalysis*. **28** (2016) 570–579. https://doi.org/10.1002/elan.201500381.

[34] X. Fan, SnO<inf>2</inf> patched ultrathin PtRh nanowires as efficient catalysts for ethanol electrooxidation, *J. Mater. Chem. A*. **7** (2019) 27377–27382. https://doi.org/10.1039/c9ta10941b.

[35] J. Thepkaew, S. Therdthianwong, A. Kucernak, A. Therdthianwong, Electrocatalytic activity of mesoporous binary/ternary PtSn-based catalysts for ethanol oxidation, *J. Electroanal. Chem.* **685** (2012) 41–46. https://doi.org/10.1016/j.jelechem.2012.09.006.

[36] K. Rahmani, B. Habibi, Excellent electro-oxidation of methanol and ethanol in alkaline media: Electrodeposition of the NiMoP metallic nano-particles on/in the ERGO layers/CE, *Int. J. Hydrogen Energy*. **45** (2020) 27263–27278. https://doi.org/10.1016/j.ijhydene.2020.07.110.

[37] C. Tian, H.X. Road, Pr ep rin t n ot pe er r Pr er ed, (n.d.).

[38] M. Ram, U. Narayan, D. Ram, P. Prasad, H. Kim, J. Hee, Hybridized bimetallic phosphides of Ni – Mo , Co – Mo , and Co – Ni in a single ultrathin-3D-nanosheets for efficient HER and OER in alkaline media, **239** (2022).

[39] L. Yang, R. Liu, L. Jiao, Electronic Redistribution : Construction and Modulation of Interface Engineering on CoP for Enhancing Overall Water Splitting, **1909618** (2020) 1–8. https://doi.org/10.1002/adfm.201909618.

[40] V.D. Jović, Calculation of a pure double-layer capacitance from a constant phase element in the impedance measurements, *Zast. Mater.* **63** (2022) 50–57. https://doi.org/10.5937/zasmat2201050J.

[41] C. Tang, N. Cheng, Z. Pu, W. Xing, X. Sun, NiSe Nanowire Film Supported on Nickel Foam : An Efficient and Stable 3D Bifunctional Electrode for Full Water Splitting ** Angewandte, (2015) 9483–9487. https://doi.org/10.1002/ange.201503407.

[42] Y. Tian, Z. Lin, J. Yu, S. Zhao, Q. Liu, J. Liu, R. Chen, Y. Qi, H. Zhang, R. Li, J. Li, J. Wang, Superaerophobic Quaternary Ni–Co–S–P Nanoparticles for Efficient Overall Water-Splitting, *ACS Sustain. Chem. Eng.* **7** (2019) 14639–14646. https://doi.org/10.1021/acssuschemeng.9b02556.

[43] V. Pe, E. Ortega, Assessment of the roughness factor effect and the intrinsic catalytic activity for hydrogen evolution reaction on Ni-based electrodeposits, **6**

(2011). https://doi.org/10.1016/j.ijhydene.2011.05.047.

[44] D. Liu, Q. Lv, D. Zheng, C. Zhou, S. Chen, K. Zhang, S. Han, H.Z. Huang, Y. Zhang, L. Chen, Strategic Design of Ethanol Oxidation Catalysts: From Active Metal Selection to Mechanistic Insights and Performance Engineering, *Nanomaterials*. **15** (2025) 1–29. https://doi.org/10.3390/nano15191477.

[45] W. Chaitree, E.E. Kalu, Co-Ni-Mo as a Non-Noble Metal Electrocatalyst for Ethanol Electro-Oxidation, *J. Electrochem. Soc.* **166** (2019) H392–H403. https://doi.org/10.1149/2.0041910jes.

[46] S. Zhou, R. Yan, W. Zhou, C. Wu, W. Cheng, Highly efficient electrooxidation of ethanol on CuPtPd trimetallic catalyst, *J. Electroanal. Chem.* **929** (2023). https://doi.org/10.1016/j.jelechem.2022.117118.

[47] Y.H. Ahmad, A.T. Mohamed, K.M. Youssef, S. Kundu, K.A. Mkhoyan, S.Y. Al-Qaradawi, Rational synthesis of ternary PtIrNi nanocrystals with enhanced poisoning tolerance for electrochemical ethanol oxidation, *Electrochem. Commun.* **101** (2019) 61–67. https://doi.org/10.1016/j.elecom.2019.03.001.

[48] H. Syafei, R. Hadawiyah, M.M. Nur, PtSnNi Trimetallic and Their Catalytic Activities in Ethanol Electrooxidation, **4** (2025) 34–42.

[49] S. Ghosh, Highly active multimetallic palladium nanoalloys embedded in conducting polymer as anode catalyst for electrooxidation of ethanol, *ACS Appl. Mater. Interfaces*. **9** (2017) 33775–33790. https://doi.org/10.1021/acsami.7b08327.